Title

Transparent Ultra-High-Loading Quantum Dot/Polymer Nanocomposite Monolith for Gamma Scintillation.

Journal

ACS nano, 11(6)

ISSN

1936-0851

Authors

Liu, Chao
Li, Zhou
Hajagos, Tibor Jacob
et al.

Publication Date

2017-06-01

DOI

10.1021/acsnano.7b02923

Peer reviewed

Transparent ultra-high-loading quantum dot/polymer nanocomposite monolith for gamma scintillation

*Chao Liu[†], Zhou Li[†], Tibor Jacob Hajagos[†], David Kishpaugh[†], Dustin Chen[†] and Qibing Pei[†]**

[†] Department of Materials Science and Engineering, Henry Samueli School of Engineering and Applied Science, University of California, Los Angeles, CA 90095, USA

KEYWORDS: quantum dots, surface modification, nanocomposites, FRET, radiation detectors.

ABSTRACT: Spectroscopic gamma-photon detection has widespread applications for research, defense, and medical purposes. However, current commercial detectors are either prohibitively expensive for wide deployment or incapable of producing the characteristic gamma photopeak. Here we report the synthesis of transparent, ultra-high-loading (up to 60 wt%) $Cd_xZn_{1-x}S$/ZnS core/shell quantum dot/polymer nanocomposite monoliths for gamma scintillation by *in situ* copolymerization of the partially mathacrylate-functionalized quantum dots in a monomer solution. The efficient Förster resonance energy transfer of the high-atomic-number quantum dots to lower-band-gap organic dyes enables the extraction of quantum-dot-borne excitons for photon production, resolving the problem of severe light yield deterioration found in previous nanoparticle-loaded scintillators. As a result, the nanocomposite scintillator exhibited simultaneous improvements in both light yield (visible photons produced per MeV of gamma

photon energy) and gamma attenuation. With these enhancements, a 662 keV Cs-137 gamma photopeak with 9.8% resolution has been detected using a 60-wt%-quantum-dot nanocomposite scintillator, demonstrating the potential of such nanocomposite system in the development of high-performance low-cost spectroscopic gamma detectors.

INTRODUCTION

Low-cost, high-performance spectroscopic γ-photon detectors have been long sought for due to their numerous applications in high-energy physics, the promotion of nuclear non-proliferation, and medical imaging.[1–3] Scintillators resolve γ energy by proportionally converting a single high-energy photon into a number of photomultiplier-tube (**PMT**) detectable low-energy photons, which is considered a more affordable solution for general purposes than delicate semiconductor detectors.[3,4] An ideal scintillator should simultaneously exhibit the following traits: 1) high atomic number (**Z**) to increase gamma attenuation and photoelectron production; 2) high light yield (**LY**, low energy photons produced per unit energy deposited, photons/MeV); 3) short emission decay lifetime; and 4) low cost and ease of large-scale fabrication. However, commercial solid-state scintillators, generally made of either inorganic single crystals or plastics, inevitably fail to meet all of these requirements due to their intrinsic material properties and limitations in fabrication processes. Nanocomposite (**NC**) scintillators composed of uniformly dispersed high-Z nanoparticles and organic dyes in a polymer matrix have been proposed to integrate the high-Z of inorganics with the fast decay and low cost of plastics, thereby improving the overall performance and cost-effectiveness.[5–11] However, most attempts were stalled at low nanoparticle loadings (<10 wt%) due to severe optical loss induced by aggregation at higher concentrations, limiting their potential for practical application.[5–7] While the use of high-Z organometallics provided an alternative for higher loading, their strong spin-orbit coupling effect necessitates careful matching

of their triplet energy levels using costly triplet emitters.[9] Recently, our group has fabricated transparent NC scintillators containing up to 60 wt% of surface-modified high-Z oxide or fluoride nanoparticles which have been used to detect a 662 keV γ photopeak.[10–13] However, in this system, the LY drastically deteriorates at higher nanoparticle loadings as the energy deposited in the non-emitting nanoparticles cannot be transported to dye sites to produce photons, limiting the loading to < 30% for practical use.[11,13]

Quantum dots (**QDs**) have been touted as a promising candidate for numerous applications such as in light emitting devices[14–16], photodetectors,[17,18] bio-labelling and imaging,[19–21] and energy harvesting[22,23] due to attractive properties such as narrow tunable emission and high photoluminescence quantum yield (**PLQY**). For NC scintillator applications, incorporation of QDs could theoretically improve the Z of NC scintillators without sacrificing their light yield due to the QDs' higher Z and PLQY.[7,8] However, severe transmittance loss in bulk NC due to QD aggregation still poses the biggest hurdle against their application as scintillators. Although the fabrication of high-loading QD/polymer NC thin films with thicknesses up to 50 μm and best transmittance of 85% at 550 nm has been reported, the scale-up to transparent bulk monoliths (at least millimeter-thick) is dramatically harder, as the transmittance loss due to Rayleigh scattering increases exponentially with the NC's thickness.[24,25] In fact, to our best knowledge, there has been no report on the fabrication of transparent millimeter-thick NCs with QD loadings exceeding 5 wt%. In addition to the transparency issue, the QDs' small Stokes shift also becomes problematic at high loadings because the severe self-absorption can easily destroy the LY of these scintillators.

In this work, by overcoming aggregation and self-absorption issues, we demonstrate the use of $Cd_xZn_{1-x}S$ (**CZS**) QDs at extremely high loadings (up to 60 wt%) in a polyvinyltoluene (**PVT**) matrix with sufficient 4,7-bis-{2'-9',9'-bis[(2''-ethylhexyl)-fluorenyl]}-2,1,3-benzothiadiazole

(**FBtF**) dyes to simultaneously improve Z and preserve LY in the resulting NC scintillators. A simple surface modification step using bis(2-(methacryloyloxy)ethyl) phosphate (**BMEP**) enables the QDs to be covalently attached to the polymerizing PVT chain, thus preventing aggregation and facilitating high transparency in the product monolith with a record-high QD loading (T_{550nm} = 65.8% for a 60 wt% QD NC monolith). Efficient Förster resonance energy transfer (**FRET**) from QDs to the lower-band-gap FBtF both suppresses QD self-absorption and promotes the extraction of QD-borne excitons to dye sites for photon production, which prevents the drastic LY deterioration found in previous NC scintillators and even improves LY for up to 11% compared to the control sample. The ultra-high loading of QD improves the Z and enabled detection of the 662 keV gamma photopeak using a QD-loaded NC scintillator. In the best demonstration, a 60 wt% CZS QD/2% FBtF/PVT NC scintillator showed a LY of 9255 photons/MeV and a photopeak resolution of 9.8% under 662 keV Cs-137 γ irradiation.

RESULTS AND DISCUSSION

Figure 1 shows a simplified schematic of the scintillation process involved in the QD/dye/polymer NC scintillator. A γ photon is first converted at QD site into a photoelectron with all energy of the photon. The photoelectron with high kinetic energy then cascades to produce a number of low-energy excitons via collisional energy exchange with the ground-state electrons on its trajectory. Depending on where the excitons are generated, they would take different FRET routes to transport and eventually be converted into visible photons at the dye sites. As dictated by the decreasing band gaps from PVT matrix (4.2 eV) to CZS QDs (2.84 eV) then to FBtF (2.56 eV), excitons generated in PVT can either be directly transferred to FBtF as shown in route 1, or to be first transferred to a nearby CZS QD as in route 3, depending on the relative proximity from the generated exciton to the closest QD and FBtF. Excitons in CZS QDs, either generated therein

(route 2) or transferred from PVT matrix (route 3), quickly decay in energy through internal conversion to its $Cd_xZn_{1-x}S$ core due to the QD's type I core/shell structure, and then transfer to FBtF via FRET. The excitons collected at FBtF sites finally recombine radiatively to produce visible photons to be detected by the PMT. It should be noted that the band structure and FRET sequences shown above should be quite generic for all efficient QD/polymer NC scintillators due to following two reasons: 1) most matrix monomers with some conjugated structures and reasonably low melting points (for the ease of fabrication) have larger band gaps than QDs with a reasonably high PLQY; 2) suppression of QD self-absorption requires the use of a lower band gap dye at rather high concentration to facilitate efficient FRET.

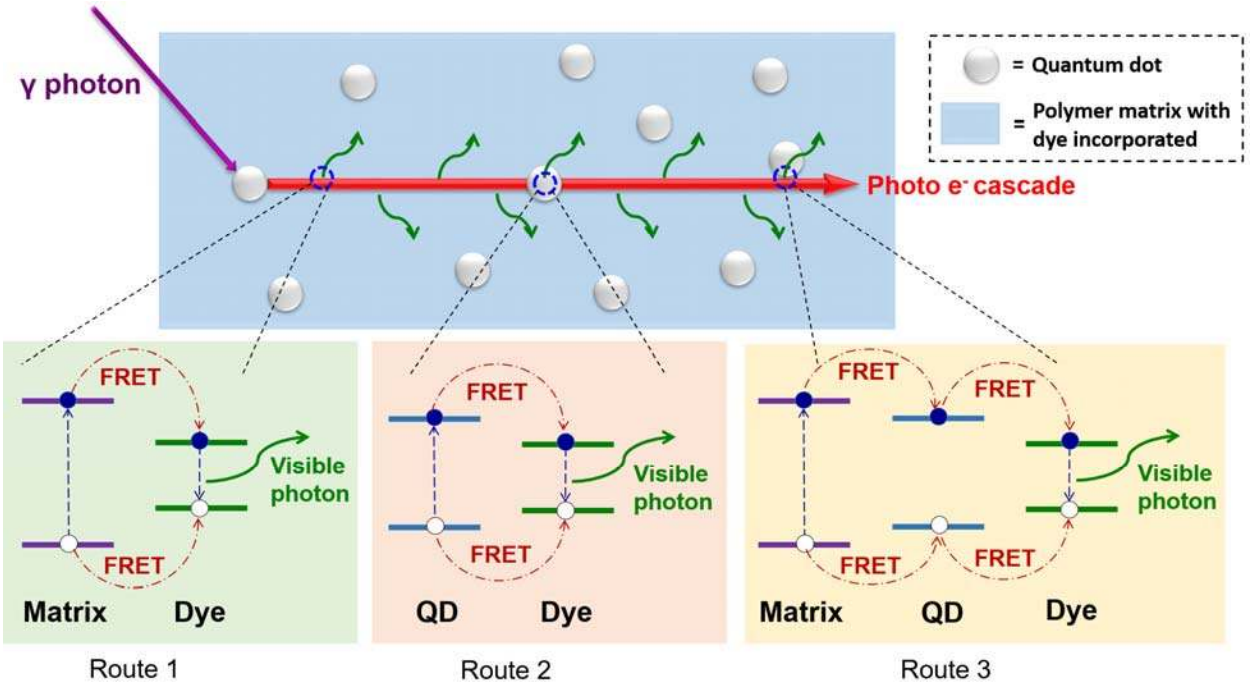

Figure 1. Schematic illustration of the scintillation process and major FRET routes involved in a QD/dye/polymer ternary system.

To realize scintillation detection using the as-described NC structure, aggregation of QDs in polymer matrix has to be minimized due to the needs for a successful out-coupling of photons and

an efficient QD-dye FRET which requires a donor-acceptor spatial proximity of 1-10 nm.[11,26] To achieve this goal, we developed a partial surface modification-*in situ* copolymerization process based on our previous work (**Figure 2a**).[11,12] The partial BMEP-modification endowed QDs with surface-grafted mathacrylate monomer groups while retaining the QD's solubility in the low-polarity VT monomer solution (detailed discussion in Supplementary Note). It should be noted that the PLQY of CZS QD decreased only slightly from 83.8% to 77.4% after partial BMEP modification, which could be ascribed to the protective ability of ZnS shell against the small amount of BMEP used. The as-modified QDs were then dissolved in VT along with FBtF and thermal initiator to form an optically clear solution. Afterwards, the solution was heated to initiate the *in situ* copolymerization, where the surface-grafted mathacrylate groups copolymerize with VT to provide covalent linkage between the QDs and polymer, thus alleviating the aggregation of QDs. As shown in **Figure 2a**, the as-fabricated NC monoliths were highly transparent with CZS QD loadings of up to 60 wt% (including surface ligand, all QD percentages from here on are weight percentages including ligand, if not specified), indicating a uniform dispersion of QDs within the matrix, which is further confirmed by transmission electron microscopy (TEM) on a focused-ion-beam etched thin film from a 60% QD NC monolith (**Figure 2b**). UV-vis transmittance test results (**Figure 2c**) confirmed the good transparencies of these ultra-high-loading NC monoliths, where the 60% QD NC monolith showed a transmittance of 65.8% at 550 nm. The slight decrease of transmittance at larger QD% and shorter wavelength is due to intensified Rayleigh scattering caused by the addition of QDs, since the refractive index of CZS QDs (>2.39 at 550 nm) is much higher than that of the PVT matrix (1.59 at 550 nm).[25] The high QD loadings in these NC monoliths were confirmed by thermogravimetric analysis (**TGA**) in air at up to 750 ^{o}C (**Figure 2d**). Considering the QD's weight loss of 35% under the same TGA

condition due to loss of ligand and conversion of $Cd_xZn_{1-x}S$ to $Cd_xZn_{1-x}O$ (Supplementary Note), the final weight percentages of 38.1%, 26.9% and 12.6% matched well with the predetermined QD loadings of 60%, 40% and 20%, confirming the efficacy of our protocol in fabricating transparent ultra-high-loading QD/polymer NC monoliths.

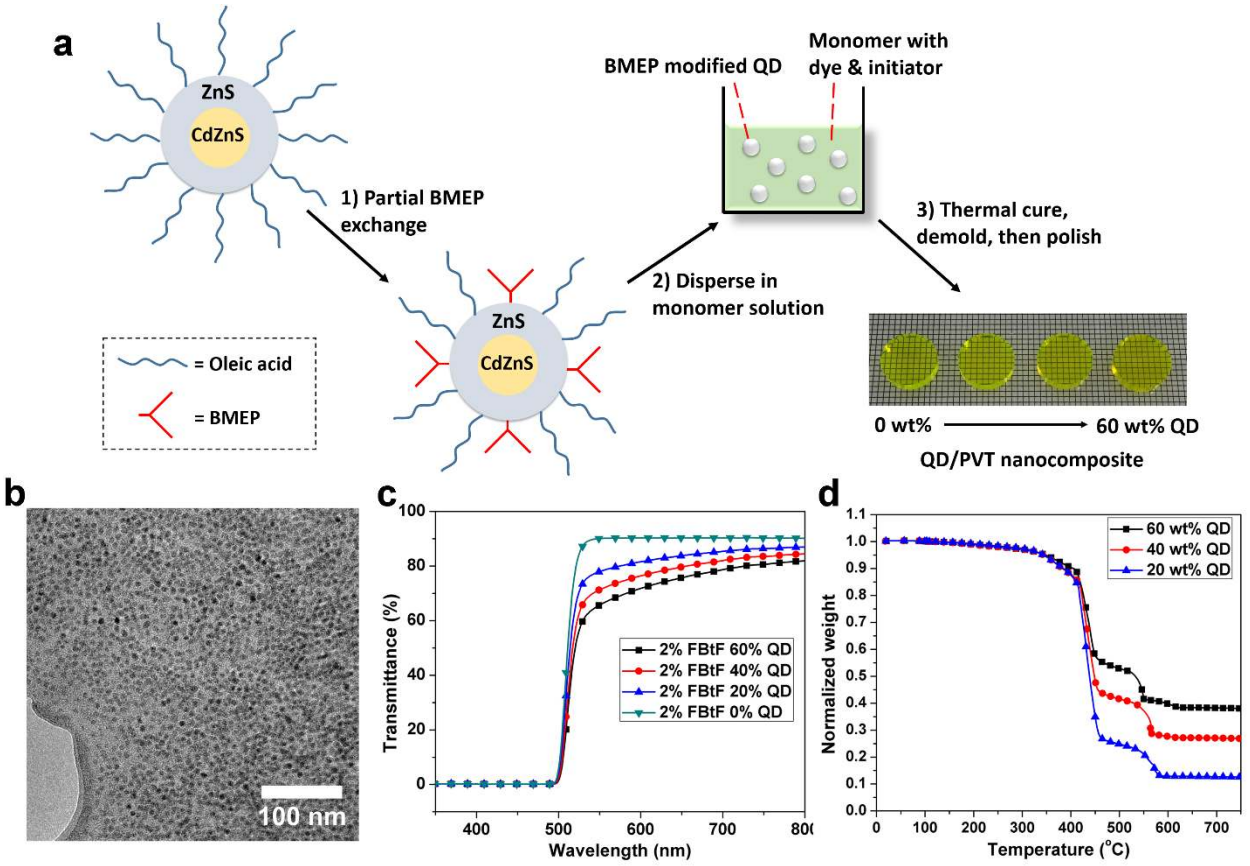

Figure 2. Transparent ultra-high-loading QD/polymer nanocomposite monoliths. a, Schematic illustration of the partial surface modification-*in situ* copolymerization process for fabricating ultra-high-loading QD/polymer NC monoliths. The last frame is a photograph of NC monoliths (2 mm thick by 1 cm diameter) with 2% FBtF and varying QD loadings from 0% to 60% at a 20 % increment. **b,** TEM image of an FIB-etched thin film from a 60 wt% QD/PVT NC monolith. Film thickness is approximately 50 nm, with the lower-left part being thinner and upper-

right thicker. **c,** UV-vis transmittance curves of the QD/PVT NC monoliths shown in **a**. **d.** TGA curves of the monoliths.

As mentioned before, a key advantage of using QDs as the high-Z additive is that their high PLQY should enable efficient conversion of energy deposited therein into detectable photons. However, severe self-absorption of QDs due to their small Stokes shift often results in drastically decreased PL at high QD concentrations, even if a small amount (0.02-0.05 wt%) of wavelength shifters are added to facilitate radiative energy transfer (detailed discussion in Supplementary Note). Therefore, to suppress QD self-absorption, organic dyes with large Stokes shift and great absorption at QD emission wavelengths were added to facilitate efficient non-radiative FRET from QDs. **Figure 3a** shows the normalized absorption and PL spectra of CZS QD and the dye, FBtF, a fluorene-derivative that has demonstrated its use as an efficient dye in our previous work.[27] The narrow violet emission of CZS QD centering at 425 nm fell exactly within the absorption peak of FBtF ($\varepsilon_{(417\ nm)} = 21595\ M^{-1}\cdot cm^{-1}$), implying a great potential for an efficient QD-to-FBtF FRET. In addition, the emission of FBtF had negligible overlap with the QD absorption, rendering both exciton back-transfer and the reabsorption of FBtF-emitted photons by QDs unlikely. These spectral characteristics suggest an efficient, unidirectional FRET from QDs to FBtF, which would alleviate QD self-absorption and help extract QD-borne excitons for photon production. It should be noted that the overall FRET rate from PVT matrix to QD and FBtF acceptors should be, if not more efficient, at least comparable to the PVT-dye FRET in traditional plastic scintillators, because 1) both FBtF and QD have very strong absorbance at PVT's emission maximum of 310 nm (**Figure S4**) and 2) the average distance from a generated exciton on PVT to the closest QD or FBtF in a 60% QD/2% FBtF NC scintillator should be much smaller compared to the case for a traditional plastic scintillator containing nothing else but 2% primary dye. For this reason, we assumed the

FRET from PVT as "efficient" and only focused on the QD-to-FBtF FRET efficiency as the key variable for scintillator performance.

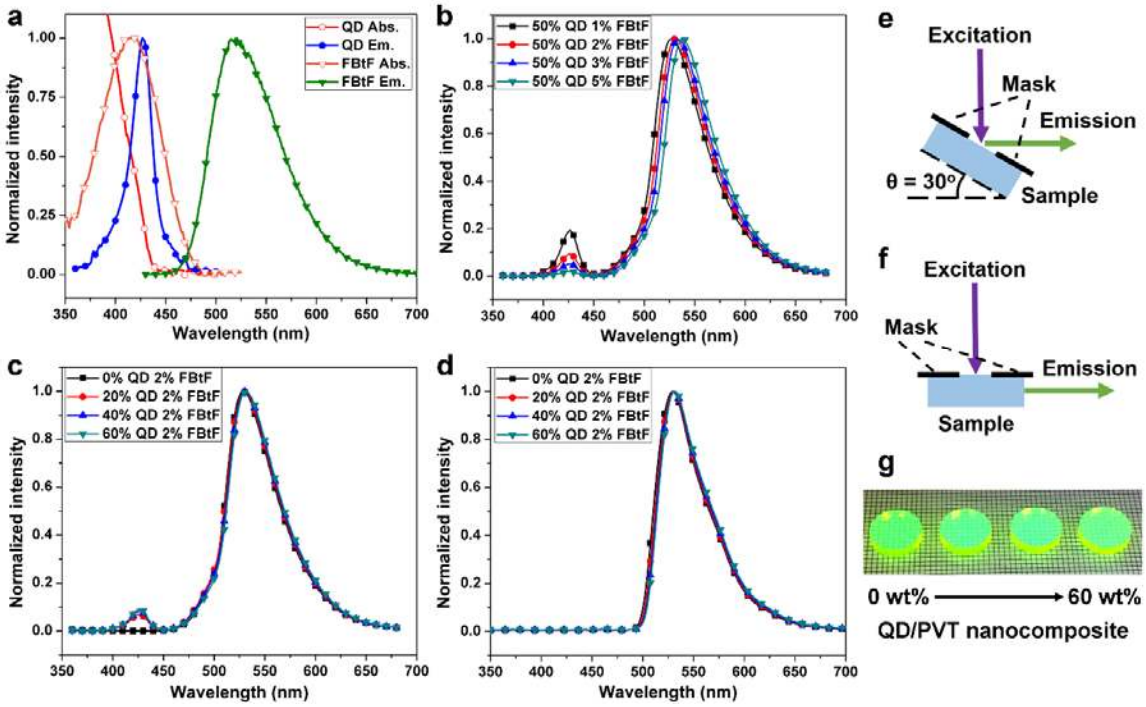

Figure 3. Photophysics characterizations of the CZS QD/FBtF/PVT NC scintillators. a, Normalized UV-vis absorbance and PL spectra ($\lambda_{exc\ QD}$ = 350 nm, $\lambda_{exc\ FBtF}$ = 420 nm) of $Cd_xZn_{1-x}S/ZnS$ core/shell quantum dot and FBtF in dilute solutions. Absorbance spectra were mass-concentration normalized, and the normalized absorbance for QDs was further multiplied by 30 to qualitatively account for the weight differences between CZS QDs and FBtF in a 60% QD/2% FBtF NC monolith. **b,c,** Normalized surface-mode PL spectra (λ_{exc} = 350 nm) of (**b**) 50% QD/1-5% FBtF/PVT NC monoliths and (**c**) 0-60% QD/2% FBtF/PVT NC monoliths. **d,** Normalized transmission-mode PL spectra (λ_{exc} = 300 nm) of 0-60% QD/2% FBtF/PVT NC monoliths. **e,f,** Schematic illustrations of the surface-mode (**e**) and transmission-mode (**f**) PL setups used in **b,c,** and **d**, respectively. **g,** Photograph of the 0-60% QD/2% FBtF/PVT NC monoliths (previously shown in **Figure 2a**) under 365 nm UV illumination.

We then used PL spectroscopy to characterize the QD-to-FBtF FRET efficiencies of NC monoliths with varying concentrations of FBtF and CZS QDs. Since efficient FRET requires a close spatial proximity (< 10 nm) between the donor QD and acceptor FBtF, a high concentration of FBtF (> 1 wt%) is needed in the NC. However, an excessively high concentration of FBtF also increases dye self-absorption in the monolith, which would decrease LY. A series of NC monoliths containing 50% QD and 1% to 5% FBtF were then fabricated to probe the optimal FBtF concentration. Due to the high concentration of FBtF, conventional right-angle setup (or transmission-mode as shown in **Figure 3f**) cannot be used to test FRET since all QD emission would eventually be absorbed by FBtF in the bulk. We then used surface-mode PL setup (**Figure 3e**) to qualitatively study the FRET efficiencies in these monoliths (Note: due to instrument limits, donor lifetime tests cannot be run at the moment to more accurately determine FRET efficiencies, see Supplementary Note). At the excitation wavelength of 350 nm, QDs are the major absorbing species in NC monoliths due to their significantly greater absorbance compared to FBtF (**Figure 3a**) and the non-absorbing PVT (E_g = 4.2 eV). Therefore, excitons were generated mainly in the QDs within a shallow layer of around 10 μm thick, as estimated using the extinction coefficient and concentration of the QDs. By comparing the QD emission to total emission intensity, FRET efficiencies could be estimated. It should be noted that this method gave only qualitative estimations, since the influence from various other processes such as absorption-reemission and scattering could hardly be excluded. As shown in **Figure 3b**, QD emission intensity decreased with the addition of FBtF, indicating an improved FRET efficiency. However, the effect of QD emission quenching diminishes at higher FBtF concentrations (**Figure S5**). This could be attributed to the saturation of FRET at high acceptor concentrations. The overall FRET efficiency $\mathbf{F_{overall}}$ from a QD to any one of its surrounding FBtF molecules can be expressed as:[26]

$$F_{overall} = \frac{\sum_i k_{ti}}{\sum_i k_{ti} + k_D} = \frac{\frac{1}{\tau_D}\sum_i \left(\frac{R_0}{R_i}\right)^6}{\frac{1}{\tau_D}\sum_i \left(\frac{R_0}{R_i}\right)^6 + \frac{1}{\tau_D}} = \frac{\sum_i \left(\frac{R_0}{R_i}\right)^6}{\sum_i \left(\frac{R_0}{R_i}\right)^6 + 1} \quad (1)$$

where k_{ti}, k_D, τ_D, R_0 and R_i are the FRET rate between QD and the *i*th nearby FBtF acceptor, radiative recombination rate of QD exciton in the absence of acceptors, fluorescence decay lifetime of QD in the absence of acceptors, characteristic FRET distance (4.02 nm as calculated in Supplementary Note), and the distance between donor QD and the *i*th FBtF molecule, respectively. At high FBtF concentrations, $\sum_i(R_0/R_i)^6 >> 1$, and $F_{overall}$ approaches 1, rendering excessive FBtF redundant. A preliminary calculation showed that $F_{overall}$ increased from 92.2% at 1% FBtF to 97.7% at 2%, confirming the as-mentioned FRET saturation (Supplementary Note). Considering the rise of FBtF self-absorption at higher concentrations, which was evident by the 10-nm-redshift of FBtF emission peak when its concentration was increased from 1% to 5%, an FBtF concentration of 2% was chosen as the optimal concentration for further fabrications and tests.

We then fabricated and tested another series of NC monoliths containing 0-60% CZS QD and 2% FBtF. As shown in **Figure 3c**, the relative intensity of QD emission remained almost identical when the QD% increased from 20% to 60%, indicating a similarly efficient QD-to-FBtF FRET with 2% FBtF. In addition, no obvious quenching of the FBtF emission was observed at larger QD%, as evident by the bright green emission of all NC monoliths under 365 nm UV illumination (**Figure 3g**). The FBtF emission only redshifted slightly from 529 to 532 nm as the QD concentration amounted to 60%, implying a similar level of self-absorption. To further study the effect of self-absorption within the bulk, transmission-mode PL spectra of these monoliths were also obtained. As shown in **Figure 3d**, similar to the surface-mode spectra, only a small redshift from 529 nm to 532 nm was observed as the QD% increased. The similar peak positions and small redshift indicated that the addition of QDs did not induce severe self-absorption by increasing

scattering within the bulk. In addition, QD emission peaks disappeared in transmission-mode PL due to complete absorption by FBtF. It should be noted that, since most photons would be generated along the fast-electron path within the bulk, these transmission-mode PL spectra should also reflect the "actual" spectra detected by PMT in scintillation tests. Therefore, transmission-mode PL spectra were used to correct the LYs with regard to PMT sensitivities, as would be shown later in this paper.

With the effective QD-to-FBtF FRET confirmed, we tested the scintillation characteristics of the ultra-high-loading QD/FBtF/PVT NC monoliths under 662 keV gamma radiation. **Figure 4a** shows the pulse-height spectra of NC monoliths containing 50% QD and 1-5% FBtF. The Compton edge was shifted significantly from 385 channels to 455 channels as the FBtF loading increased from 1% to 2%, displaying an improvement of 15.4% in apparent LY. However, further increase of FBtF loading from 2% to 5% saw no obvious change in LY. Such trend in LY change could be ascribed to the competition between FRET and self-absorption. The initial LY increase at 2% FBtF could be ascribed to the significantly improved FRET efficiency compared to 1% FBtF as discussed before. However, adding more FBtF only improves FRET meagerly, which could be offset by the steadily intensified self-absorption, resulting in the stagnation of LY. The balance between FRET improvement and self-absorption therefore made 2% FBtF the optimal concentration. Pulse-height spectra of NC monoliths containing 2% FBtF and 0-60% of CZS QDs were shown in **Figure 4b**. LY of the NC monoliths did not decrease drastically at larger QD% as in the case with non-emitting nanoparticle.[11,13] In contrast, we observed a slight increase of LY from 0 to 40 wt% QD loadings, and a more significant increase at 60% QD loading. By comparing the Compton Edge to that of a standard EJ212 sample and correcting the PMT sensitivity difference (**Figure S6**), we have obtained the absolute LYs of the 0-60% QD/2% FBtF NC

scintillators (See Supplementary Method for more details). As shown in **Figure 4c**, the LY increased from 8340 photons/MeV for the bare 2% FBtF/PVT scintillator to 8528, 8714 and 9275 photons/MeV for the NC scintillators containing 20%, 40% and 60% QD, respectively, demonstrating a maximum of 11.2% improvement in LY. To find out the reason for this improved LY, we first wrote out the LY of a composite system as:[4,11]

$$LY = \left(\sum_j E_j \times P_j \times F_j\right) \times \Phi_{dye} \times \left(1 - A_{dye}\right) \quad (2)$$

where E_j, P_j, F_j, Φ_{dye} and A_{dye} denote the percentage of fast-electron energy deposited in component j as previously defined by us in Ref. 11 (j = QD, matrix or ligand. Note: this is a simplified model, a more detailed discussion could be found in Ref. 28 by Bulin *et al.*),[11,28] exciton productivity of component j under fast-electron excitation (number of excitons generated per unit of fast electron energy deposited, excitons/MeV), overall efficiency of exciton transfer from component j to dye site, PLQY of dye, and self-absorption loss of dye emission (the ratio between photons lost due to self-absorption and photons produced), respectively. Among the five factors, Φ_{dye} should remain constant regardless of QD%, while A_{dye} should increase with QD% due to intensified scattering and result in a lower LY. Since E_j is not an intrinsic property dictating exciton and photon production, the increase in LY should then be ascribed to a larger product of P_j and F_j for QD compared to the matrix, as this product for the aliphatic ligands should be close to zero due to their negligible PLQY.[4,11,13] As discussed before, FRET for excitons generated in QD and matrix should both be efficient with 2% FBtF. Therefore, the higher LY for QD/PVT NC scintillator should be mainly attributed to a larger P_j of QD compared to that of PVT. Assuming $F_{QD} = F_{Matrix}$, $P_{Ligand} \times F_{Ligand} = 0$, and no absorption loss, i.e. $A_{dye} = 0$, we have obtained $P_{QD} = 1.3 \times P_{Matrix}$ using E_j's calculated as described in a previous paper, indicating a 30% higher exciton productivity.[11] Greater exciton productivities of inorganic materials due to their smaller ionization energies had been

proposed before to account for the higher LYs of inorganic scintillators; however, the exact reasons behind this still remained unknown.[4,6,8] More research, both theoretical and experimental, is needed to unravel the puzzle.

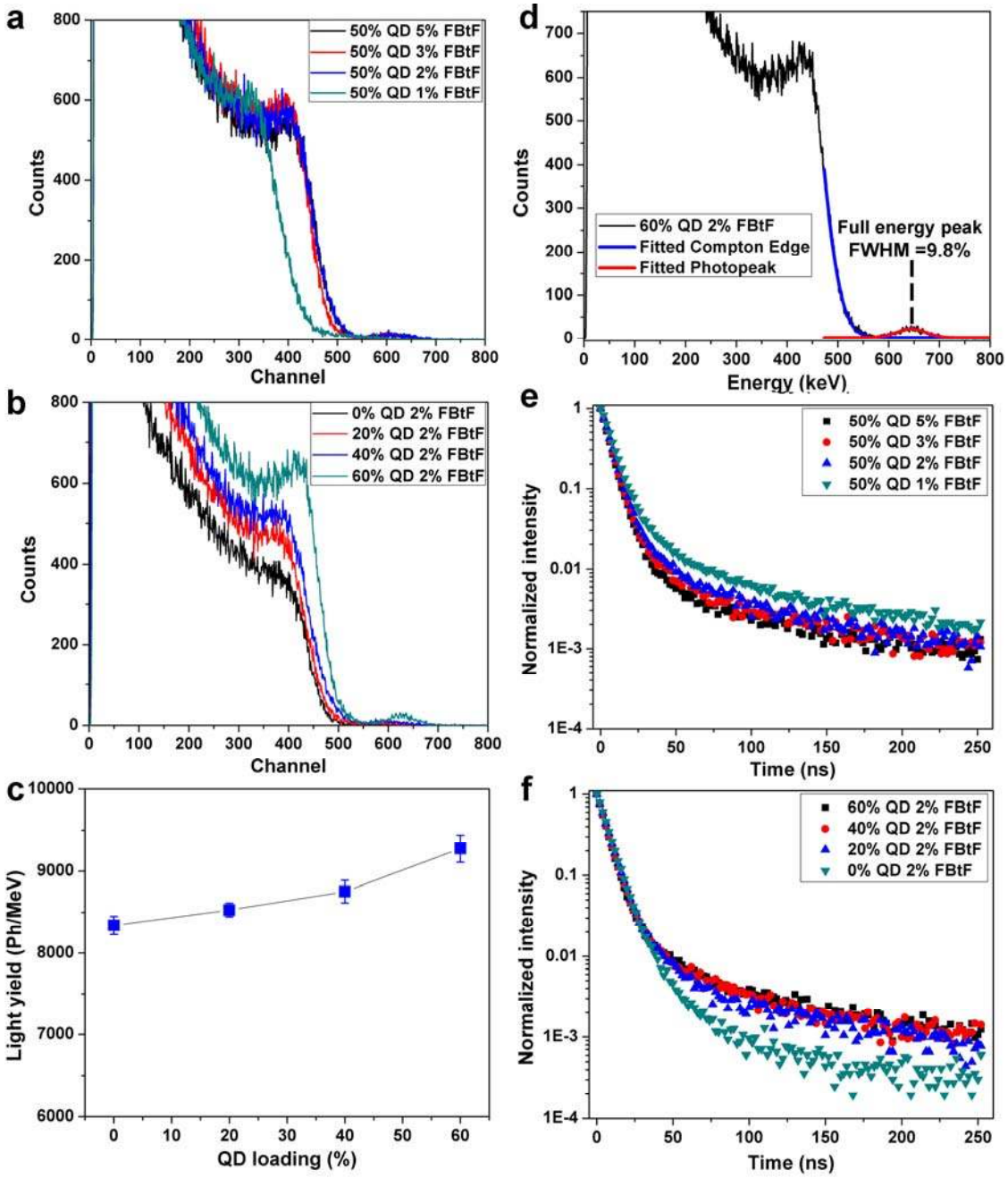

Figure 4. Cs-137 gamma-ray scintillation using the ultra-high-loading QD/polymer NC monoliths. a,b, Pulse height spectra of (**a**) 50% QD/1-5% FBtF/PVT NC monoliths and (**b**) 0-

60% QD/2% FBtF/PVT NC monoliths. **c,** Chart of scintillation light yields of the 0-60% QD/2% FBtF/PVT nanocomposites after PMT spectral sensitivity correction, error bars indicate one standard deviation after three independent tests. **d,** Energy correlated pulse height spectrum with fitted Compton edge and full-energy peak for a 2-mm-thick 60% QD/2% FBtF/PVT NC monolith. **e,f,** Radioluminescence decay curves of (**e**) 50% QD/1-5% FBtF/PVT NC monoliths and (**f**) 0-60% QD/2% FBtF/PVT NC monoliths.

The addition of QDs also improved the Z of NC scintillators, which enabled the detection of photopeak in the pulse-height spectra. **Figure 4d** shows the energy correlated pulse-height spectrum obtained using the 60% QD/2% FBtF/PVT NC scintillator. A full-energy peak centering at 646 keV with 9.8% resolution was observed. The small offset of 16 keV from 662 keV is due to the existence of an inseparable Cd Kα escape peak located at 639 keV, which should be eliminated at larger scintillator sizes. The energy resolution of 9.8% is not superior to previous blue-emitting scintillators, which is due to the green-emitting scintillator's lower apparent LY as-detected by the PMT.[11,13] However, it is still much better than the reported 11.4% resolution of FBtF-loaded Gd_2O_3 NC scintillators, confirming the improved LY by adding QDs.[10] It is expected that, by using the more green-sensitive Si photomultiplier for photon detection, the spectral mismatch could be eliminated, which should greatly enhance the apparent LYs and resolutions.[29] Moreover, with the adoption of such detectors, other higher Z quantum dots with longer-wavelength emissions could also be employed to make nanocomposite scintillators, thereby improving the photopeak-to-Compton-edge ratio.

In addition to the enhanced LY and Z, another promising feature of the QD/polymer NC scintillators is their retained short scintillation lifetimes. **Figure 4e and 4f** show the radioluminescence decay curves of 50% QD/1-5% FBtF/PVT and 0-60% QD/2% FBtF/PVT NC

scintillators, respectively. The curves were fitted using a double exponential function with the results listed in **Table S1** (fitting details in Supplementary Note). All NC scintillators displayed a dominating fast emission with around 7 ns lifetimes, which was from FBtF as evident from the 2% FBtF/PVT sample. The lifetime of this fast component decreased with increasing FBtF% or NP%, which could be ascribed to an intensified FBtF self-absorption due to higher dye loading or enhanced scattering, respectively. In addition to the fast component, a minor slow component with around 70 ns lifetimes was also observed. The intensity of this slow emission increased with additional QD but decreased at higher FBtF%. In addition, the lifetime of slow decay decreased at higher FBtF% and QD%. Since the typical PL lifetime of CZS core/shell QD is around 10-15 ns, which should further be significantly reduced due to strong FRET to FBtF, the slow component should not come from direct QD emission.[26,30,31] However, the increased intensity at higher QD% and lower FBtF% also suggest that the slow component originates from the addition of QD. It is therefore assumed that the slow decay might be related with some nonlinear processes of QD. Effects such as triplet-triplet annihilation and delayed fluorescence had been reported on plastic scintillators with high primary dye loadings, which might also be applied to this case since QDs could also be viewed as a primary dye.[3,4,32] More research is underway to address the slow emission, which might find application in γ/neutron pulse-shape discrimination.

CONCLUSION

In summary, transparent ultra-high-loading CZS QD/FBtF/PVT NC scintillators have been successfully synthesized via *in situ* polymerization of the monomer solution containing partial BMEP-modified QDs. By facilitating effective QD-dye FRET, simultaneous enhancements in both Z and LY in a NC scintillator have been achieved for the first time, rendering it no longer necessary to sacrifice LY for Z improvements in the nanoparticle-based NC systems. The detection

of a 662 keV Cs-137 photopeak with 9.8% resolution using commercial PMT has been demonstrated using a prototype NC scintillator, highlighting the great potential for such QD/dye/polymer NC system in radiation spectroscopy. Following the general structure built in this work, future efforts will be focused on the integration of more advanced green/red-sensitive photodetectors such as the Si photomultiplier, which should facilitate the utilization of a greatly expanded family of QDs with both higher Z and PLQY to further improve the performance of NC scintillators. In addition, follow-up investigations are also underway to elucidate the origin of LY enhancement and slow emission component from QD addition, which could lead to new discoveries and applications in γ/neutron pulse-shape discrimination. Other than the radiation detection use, the facile fabrication of stable, uniform QD/polymer nanocomposites might also find great potential in other fields such as in solar concentrators and optoelectronic applications.

METHODS

Materials Cadmium oxide (99.99% trace metal basis), zinc acetate (99.99% trace metal basis), oleic acid (technical grade, 70%), 1-octadecene(technical grade, 90%), sulfur (99.998% trace metal basis), tributylphosphine(97%), bis(2-(methacryloyloxy)ethyl) phosphate (**BMEP**), methylstyrene (commonly referred to as vinyltoluene, **VT**, 99%), divinylbenzene (**DVB**, technical grade, 80%), 1,4-bis(5-phenyl-2-oxazolyl)benzene (**POPOP**), and Luperox 231 (92%) were purchased from Sigma Aldrich. All common solvents used were ACS grade, while solvents used for spectroscopy were HPLC grade. VT and DVB were purified by a mini column packed with inhibitor removers to remove *tert*-butylcatechol before use. An Eljen-212 general-purpose plastic scintillator was obtained from Eljen Technology and was polished into a disk with dimensions 10 mm in diameter and 2 mm thickness to serve as the standard for scintillation measurements. 4,7-bis-{2'-9',9'-bis[(2''-ethylhexyl)-fluorenyl]}-2,1,3-benzothiadiazole (**FBtF**) was synthesized

according to a previous protocol developed in our lab (details in Supplementary Methods).[27,33] $Cd_xZn_{1-x}S/ZnS$ core-shell QDs were synthesized following a well-developed protocol (details in Supplementary methods).[16] All other materials were used as received.

Fabrication of ultra-high-loading QD/PVT NC monoliths Surface modification of the QDs was performed following a similar protocol described previously.[12] In a typical experiment, 1000 mg of QDs were precipitated from the toluene stock solution using EtOH. The QDs were then dissolved in 14 mL of $CHCl_3$ to form a clear solution, into which 89 mg of BMEP in 2 mL $CHCl_3$ was added drop-wise under rigorous stirring. The reaction mixture was left stirring overnight and then filtered through a 200-nm pore-size PTFE syringe filter to remove the minimal precipitates generated during the reaction. The as-filtered solution was first concentrated using rotary evaporation and then washed twice with 3:1 acetone/toluene, followed by washing another two times with 3:1 acetone/hexane. The washed NPs were sonicated to disperse in a VT solution containing 5 vol% DVB and 0.1 vol% Luperox 231. The clear solution was then brought into a nitrogen-protected glove box and mixed with 1-5 wt% of FBtF in 10 mm diameter glass vials, followed by thermal curing at 95 ºC for 24 hours. After curing, the resulting monoliths were removed from the glass vials and polished for further characterizations.

Characterizations TEM images were taken using an FEI T12 Quick CryoEM and CryoET microscope operated at 120 keV. The nanocomposite thin-film TEM samples were prepared by focused ion beam etching of the monolith using an FEI Nova 600 SEM/FIB system. Powder X-ray diffraction data was obtained using a Bruker D8 Discover powder x-ray diffractometer with Cu Kα radiation. Fourier transform infrared spectra were obtained using a Jasco 420 FTIR spectrophotometer. FTIR samples were prepared by applying a drop of QD solution (around 50 mg/mL) onto a Real Crystal KBr IR sample card followed by drying in air. Energy dispersive X-

ray spectroscopy (**EDX**) was performed on an FEI Nova Nano 230 scanning electron microscope operated at 10 keV. The EDX samples were first dispersed in corresponding solvents and then drop-casted onto Cu tape, followed by drying under high vacuum. UV-visible tests were performed on a Shimadzu UV-1700 spectrophotometer. Homemade masks were applied to reduce the variations in light paths for monolith transmittance tests. TGA was performed on a Perkin Elmer Diamond Thermogravimetric/Differential Thermal Analyzer. The sample was first stabilized at 100 ºC for 10 min to remove residue solvents and water before being heated to 750 ºC in air at a ramping rate of 10 ºC/min, followed by an isothermal process at 750 ºC for another 20 min to ensure complete decomposition. Photoluminescence spectra were obtained with a PTI QuantaMaster 30 spectrofluorometer. Solution-sample emissions were acquired using 10 mm quartz cells in the standard right-angle geometry, whereas monoliths were mounted on a homemade rotation stage with masks for tests in different geometries. Photoluminescence quantum yields (**PLQY**) of the QDs in toluene were measured by the relative method as described in an IUPAC technical report, with POPOP in cyclohexane (PLQY = 0.97) serving as the reference standard.[34] In short, photoluminescence (under 350 nm excitation) and absorbance spectra were recorded for a series of dilute solutions with different concentrations. The integrated PL intensities were plotted against the absorbance at 350 nm for both QD and POPOP solutions. PLQY of the QD were given by:

$$\Phi_{QD} = \Phi_{POPOP}\left(\frac{Grad_{QD}}{Grad_{POPOP}}\right)\left(\frac{n_{QD}^2}{n_{POPOP}^2}\right)$$

where Φ, Grad, n are the PLQY, slope of the curve for integrated PL intensity vs. absorbance, and refractive index of the solvent, respectively.

Gamma scintillation measurement Gamma scintillation measurement was performed using a home-built system in a dark box as described in our previous papers.[11,32] In a typical measurement,

a 1-cm-diameter 2-mm-thick sample was first placed in a customized PTFE sample holder and then coupled to a Hamamatsu R878 PMT using optical grease. A Cs-137 source (662 keV characteristic γ energy) of 10 μCi activity (3.7 x 10^5 decays/second) was then placed right outside the PTFE sample holder. The PTFE sample holder with a relatively rough surface is used as a diffuse reflector to optimize photon collection by PMT while also serves to exclude the influence of concomitantly emitted β rays from the Cs source. The PMT was equilibrated for 30 min after sealing the dark box. Typical acquisition live time was set as one hour. The signal was recorded by a Canberra Lynx multichannel analyzer with rise time and flat top time set to 1 μs and 0.5 μs, respectively. Light yields of the scintillators were obtained by the commonly used protocol of first comparing the sample's Compton edge channel number to that of a standard EJ-212 sample tested under the same conditions, followed by correction with regard to the PMT's spectral sensitivity using the as-obtained transmission-mode PL spectra, where the typical standard deviation is smaller than 2%.[35–37] In this manner, the light yields were calculated using the following formula:

$$LY_{NC} = LY_{EJ-212}\left(\frac{CE_{NC}}{CE_{EJ-212}}\right)\left(\frac{\phi_{EJ-212}}{\phi_{NC}}\right)$$

where LY, CE, and ϕ represent the light yield, channel number of the Compton edge, and the PMT-sensitivity correction factor, respectively. A light yield of 10,000 photons/MeV for EJ-212 was used per the product specification. The PMT-sensitivity correction factor ϕ_x for sample *x* was computed using the following formula:

$$\phi_x = \frac{\int \varphi(\lambda)\, I_x(\lambda) d\lambda}{\int I_x(\lambda) d\lambda}$$

where φ(λ) and $I_x(\lambda)$ are the PMT's quantum efficiency and the sample's emission intensity at wavelength λ, respectively. As the quantum efficiency of PMT varies drastically over the

emission spectrum of FBtF (**Figure S6**), a peak-emission redshift per nm will bring an additional 2 to 2.5% increase in absolute light yield.

Time resolved radioluminescence decay lifetime measurement Time resolved radioluminescence decay curves were measured using a home-built time-correlated single photon counting (**TCSPC**) system described in our previous paper.[32] The measurement uses a Hamamatsu H2431-50 assembly as the start PMT and a Hamamatsu H10721P-110 module fitted with an E5776-51 SMA fiber optic adapter as the stop PMT. The sample was placed in a homemade PTFE sample holder and directly coupled to the start PMT using optical grease, with a bare terminated 800 μm multi-mode fiber inserted through a tightly fitting hole on the PTFE sample holder to conduct single photons from the sample to the stop PMT. The 10 μCi Cs-137 source was then placed near the PTFE sample holder. Similarly, the PMTs were equilibrated for 30 min after the dark box was sealed. Signal from the stop PMT was fed into an Ortec Model 9326 fast preamplifier, and the resulting output along with the signal from the start PMT was digitized using a PicoScope Model 5244B oscilloscope (Pico Technology, Inc.). The differences in arrival times between the main pulses detected by the start PMT and the single photon pulses detected by the stop PMT were histogrammed to obtain the scintillation decay curves over a 250-ns interval.

ASSOCIATED CONTENT

Supporting Information. Additional experimental details and discussions, characterization results such as TEM, XRD, TGA, FTIR, PL, and fitted radioluminescence lifetimes. This material is available free of charge via the Internet at http://pubs.acs.org.

AUTHOR INFORMATION

Corresponding Author

* qpei@seas.ucla.edu

Author Contributions

The manuscript was written through contributions of all authors. All authors have given approval to the final version of the manuscript.

Notes

The authors declare no competing financial interest.

ACKNOWLEDGMENT

The authors would like to thank Dr. Nerine Cherepy and Dr. Stephen Payne of the Lawrence Livermore National Laboratory for kindly sharing their knowledge and insights on scintillation photophysics and measurement techniques. This work was financially supported by the Defense Threat Reduction Agency (DTRA) under the contract HDTRA1-14-1-0032. The authors thank Dr. Noah Bodzin at the UCLA Nanoelectronics Research Facility for his help in FIB sample preparation. C.L. appreciates the valuable discussions and comments from Dr. Xiaofeng Liu and Dr. Fangchao Zhao. The authors acknowledge the use of instruments at the Electron Imaging Center for NanoMachines supported by NIH (1S10RR23057 to ZHZ) and CNSI at UCLA.

REFERENCES

(1) Milbrath, B. D.; Peurrung, A. J.; Bliss, M.; Weber, W. J. Radiation Detector Materials: An Overview. *J. Mater. Res.* **2011**, *23*, 2561–2581.

(2) Van Eijk, C. W. E. Inorganic Scintillators in Medical Imaging. *Phys. Med. Biol.* **2002**, *47*, R85–R106.

(3) Knoll, G. F. *Radiation Detection and Measurement*; 4th ed.; John Wiley & Sons: Hoboken, 2010.

(4) Birks, J. B. *The Theory and Practice of Scintillation Counting*; Pergamon: Oxford, England, 1964.

(5) McKigney, E. A.; Del Sesto, R. E.; Jacobsohn, L. G.; Santi, P. A.; Muenchausen, R. E.; Ott, K. C.; McCleskey, T. M.; Bennett, B. L.; Smith, J. F.; Cooke, D. W. Nanocomposite Scintillators for Radiation Detection and Nuclear Spectroscopy. *Nucl. Instrum. Methods Phys. Res., Sect. A* **2007**, *579*, 15–18.

(6) Létant, S. E.; Wang, T.-F. Semiconductor Quantum Dot Scintillation under Gamma-Ray Irradiation. *Nano Lett.* **2006**, *6*, 2877–2880.

(7) Kang, Z.; Zhang, Y.; Menkara, H.; Wagner, B. K.; Summers, C. J.; Lawrence, W.; Nagarkar, V. CdTe Quantum Dots and Polymer Nanocomposites for X-Ray Scintillation and Imaging. *Appl. Phys. Lett.* **2011**, *98*, 181914.

(8) Campbell, I. H.; Crone, B. K. Quantum-Dot/Organic Semiconductor Composites for Radiation Detection. *Adv. Mater.* **2006**, *18*, 77–79.

(9) Rupert, B. L.; Cherepy, N. J.; Sturm, B. W.; Sanner, R. D.; Payne, S. A. Bismuth-Loaded Plastic Scintillators for Gamma-Ray Spectroscopy. *Europhys. Lett.* **2012**, *97*, 22002.

(10) Cai, W.; Chen, Q.; Cherepy, N.; Dooraghi, A.; Kishpaugh, D.; Chatziioannou, A.; Payne, S.; Xiang, W.; Pei, Q. Synthesis of Bulk-Size Transparent Gadolinium Oxide–polymer Nanocomposites for Gamma Ray Spectroscopy. *J. Mater. Chem. C* **2013**, *1*, 1970.

(11) Liu, C.; Hajagos, T. J.; Kishpaugh, D.; Jin, Y.; Hu, W.; Chen, Q.; Pei, Q. Facile Single-Precursor Synthesis and Surface Modification of Hafnium Oxide Nanoparticles for Nanocomposite γ-Ray Scintillators. *Adv. Funct. Mater.* **2015**, *25*, 4607–4616.

(12) Jin, Y.; Kishpaugh, D.; Liu, C.; Hajagos, T. J.; Chen, Q.; Li, L.; Chen, Y.; Pei, Q. Partial Ligand Exchange as a Critical Approach to the Synthesis of Transparent Ytterbium Fluoride–polymer Nanocomposite Monoliths for Gamma Ray Scintillation. *J. Mater. Chem. C* **2016**, *4*, 3654–3660.

(13) Chen, Y.; Liu, C.; Jin, Y.; Hajagos, T. J.; Kishpaugh, D.; Zhuang, Q.; Pei, Q. Ytterbium Fluoride Loaded Plastic Scintillators for γ-Ray Spectroscopy. In *Proc. SPIE 9968, Hard X-Ray, Gamma-Ray, and Neutron Detector Physics XVIII*; 2016; p. 99680N.

(14) Dai, X.; Zhang, Z.; Jin, Y.; Niu, Y.; Cao, H.; Liang, X.; Chen, L.; Wang, J.; Peng, X. Solution-Processed, High-Performance Light-Emitting Diodes Based on Quantum Dots. *Nature* **2014**, *515*, 96–99.

(15) Shirasaki, Y.; Supran, G. J.; Bawendi, M. G.; Bulović, V. Emergence of Colloidal Quantum-Dot Light-Emitting Technologies. *Nat. Photonics* **2012**, *7*, 13–23.

(16) Yang, Y.; Zheng, Y.; Cao, W.; Titov, A.; Hyvonen, J.; Manders, J. R.; Xue, J.; Holloway, P. H.; Qian, L. High-Efficiency Light-Emitting Devices Based on Quantum Dots with Tailored Nanostructures. *Nat. Photonics* **2015**, *9*, 1–9.

(17) Bao, J.; Bawendi, M. G. A Colloidal Quantum Dot Spectrometer. *Nature* **2015**, *523*, 67–70.

(18) Konstantatos, G.; Howard, I.; Fischer, A.; Hoogland, S.; Clifford, J.; Klem, E.; Levina, L.; Sargent, E. H. Ultrasensitive Solution-Cast Quantum Dot Photodetectors. *Nature* **2006**, *442*, 180–183.

(19) Medintz, I. L.; Uyeda, H. T.; Goldman, E. R.; Mattoussi, H. Quantum Dot Bioconjugates for Imaging, Labelling and Sensing. *Nat. Mater.* **2005**, *4*, 435–446.

(20) Clapp, A. R.; Medintz, I. L.; Mauro, J. M.; Fisher, B. R.; Bawendi, M. G.; Mattoussi, H. Fluorescence Resonance Energy Transfer Between Quantum Dot Donors and Dye-Labeled Protein Acceptors. *J. Am. Chem. Soc.* **2004**, *126*, 301–310.

(21) Chan, W. C. W.; Nie, S. Quantum Dot Bioconjugates for Ultrasensitive Nonisotopic Detection. *Science* **1998**, *281*, 2016–2018.

(22) Meinardi, F.; McDaniel, H.; Carulli, F.; Colombo, A.; Velizhanin, K. a.; Makarov, N. S.; Simonutti, R.; Klimov, V. I.; Brovelli, S. Highly Efficient Large-Area Colourless Luminescent Solar Concentrators Using Heavy-Metal-Free Colloidal Quantum Dots. *Nat. Nanotechnol.* **2015**, *10*, 878–885.

(23) Nozik, A. J. Quantum Dot Solar Cells. *Physica E Low Dimens. Syst. Nanostruct.* **2002**, *14*, 115–120.

(24) Zhu, M.; Peng, X.; Wang, Z.; Bai, Z.; Chen, B.; Wang, Y.; Hao, H.; Shao, Z.; Zhong, H. Highly Transparent and Colour-Tunable Composite Films with Increased Quantum Dot Loading. *J. Mater. Chem. C* **2014**, *2*, 10031–10036.

(25) Lü, C.; Yang, B. High Refractive Index Organic–inorganic Nanocomposites: Design, Synthesis and Application. *J. Mater. Chem.* **2009**, *19*, 2884.

(26) Lakowicz, J. R. *Principles of Fluorescence Spectroscopy*; 3rd ed.; Springer: New York, 2006.

(27) Kishpaugh, D.; Hajagos, T. J.; Liu, C.; Chen, Q.; Pei, Q. Applications of Fluorene Moiety Materials to Improved Plastic Green Scintillators. Manuscript submitted.

(28) Bulin, A.-L.; Vasil'ev, A.; Belsky, A.; Amans, D.; Ledoux, G.; Dujardin, C. Modelling Energy Deposition in Nanoscintillators to Predict the Efficiency of the X-Ray-Induced Photodynamic Effect. *Nanoscale* **2015**, *7*, 5744–5751.

(29) Grodzicka, M.; Moszynski, M.; Szczesniak, T.; Kapusta, M.; Szawlowski, M.; Wolski, D. Energy Resolution of Scintillation Detectors with SiPM Light Readout. *IEEE Nucl. Sci. Symp. Conf. Rec.* **2010**, 1940–1948.

(30) Wang, Y.; Leck, K. S.; Ta, V. D.; Chen, R.; Nalla, V.; Gao, Y.; He, T.; Demir, H. V.; Sun, H. Blue Liquid Lasers from Solution of CdZnS/ZnS Ternary Alloy Quantum Dots with Quasi-Continuous Pumping. *Adv. Mater.* **2015**, *27*, 169–175.

(31) Lee, K. H.; Lee, J. H.; Kang, H. D.; Han, C. Y.; Bae, S. M.; Lee, Y.; Hwang, J. Y.; Yang, H. Highly Fluorescence-Stable Blue CdZnS/ZnS Quantum Dots against Degradable Environmental Conditions. *J. Alloys Compd.* **2014**, *610*, 511–516.

(32) Hajagos, T. J.; Kishpaugh, D.; Pei, Q. Pulse Shape Discrimination Properties of Plastic Scintillators Incorporating a Rationally Designed Highly Soluble and Polymerizable Derivative of 9, 10-Diphenylanthracene. *Nucl. Instrum. Methods Phys. Res., Sect. A* **2016**, *825*, 40–50.

(33) Chen, Q. Polymer Composites for Radiation Scintillati*on*, *Electronic Theses and Dissertations,University of California, Los Angeles.* **2012**.

(34) Brouwer, A. M. Standards for Photoluminescence Quantum Yield Measurements in Solution (IUPAC Technical Report). *Pure Appl. Chem.* **2011**, *83*, 2213–2228.

(35) Zaitseva, N.; Rupert, B. L.; PaweŁczak, I.; Glenn, A.; Martinez, H. P.; Carman, L.; Faust, M.; Cherepy, N.; Payne, S. Plastic Scintillators with Efficient Neutron/gamma Pulse Shape Discrimination. *Nucl. Instrum. Methods Phys. Res., Sect. A* **2012**, *668*, 88–93.

(36) Hristova, A. V.; Vapirev, E. I.; Tsankov, L. T.; Jordanov, V. Compton Edge Energy Calibration of Organic Detectors. *Int. J. Radiat. Appl. Instrumentation. Part A. Appl. Radiat. Isot.* **1990**, *41*, 887–889.

(37) van Loef, E. V.; Markosyan, G.; Shirwadkar, U.; Shah, K. S. Advanced Plastic Scintillators with Pulse Shape Discrimination. In *2012 IEEE Nuclear Science Symposium and Medical Imaging Conference Record (NSS/MIC)*; IEEE, 2012; pp. 1974–1977.

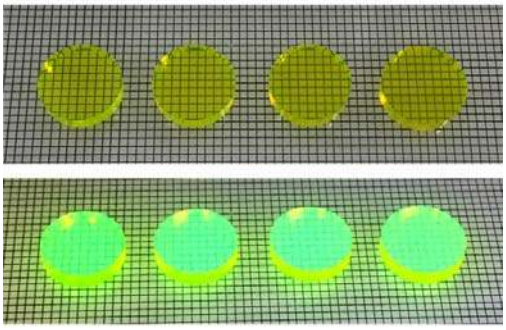

Table of Contents